nature neuroscience

RESOURCE

https://doi.org/10.1038/s41593-020-0703-x

Live-imaging of astrocyte morphogenesis and function in zebrafish neural circuits

Jiakun Chen[1]✉, Kira E. Poskanzer[2,3], Marc R. Freeman[1] and Kelly R. Monk[1]✉

How astrocytes grow and integrate into neural circuits remains poorly defined. Zebrafish are well suited for such investigations, but bona fide astrocytes have not been described in this system. Here we characterize a zebrafish cell type that is remarkably similar to mammalian astrocytes that derive from radial glial cells and elaborate processes to establish their territories at early larval stages. Zebrafish astrocytes associate closely with synapses, tile with one another and express markers, including *Glast* and glutamine synthetase. Once integrated into circuits, they exhibit whole-cell and microdomain Ca^{2+} transients, which are sensitive to norepinephrine. Finally, using a cell-specific CRISPR–Cas9 approach, we demonstrate that *fgfr3* and *fgfr4* are required for vertebrate astrocyte morphogenesis. This work provides the first visualization of astrocyte morphogenesis from stem cell to post-mitotic astrocyte in vivo, identifies a role for Fgf receptors in vertebrate astrocytes and establishes zebrafish as a valuable new model system to study astrocyte biology in vivo.

Glial cells are critical regulators of nervous system development and function. Glia constitute at least half of the cells in the human brain, and astrocytes are the most abundant glial cell type in the mammalian central nervous system (CNS). Astrocytes are unusually elaborate cells, and much of their functional associations depend on their highly branched morphology. They extend many fine cellular processes to interact closely with synapses, neuronal cell bodies, axons, blood vessels and other glial cells in the CNS. Through these associations, they fulfill diverse functions to support and enhance neuronal activity, maintain CNS homeostasis and modulate neural circuits[1,2]. However, it remains poorly understood how astrocytes are specified, how they develop their intricate morphological associations, how astrocyte–neighbor interactions influence in vivo functional roles and how diverse their functions might be in different brain regions. Given the growing number of studies demonstrating direct roles for astrocytes in regulating neural circuit function[3,4], it is of particular interest to understand how astrocyte–synapse interactions modulate synaptic and circuit function. Astrocyte dysfunction has also been implicated in an array of neurological diseases[5], although the mechanisms by which changes in astrocyte physiology lead to disease require considerable further study.

Most understanding of astrocyte biology derives from investigation of rodent models, where the molecular and morphological features of astrocytes are well described. There appears to be a striking conservation of astrocyte biology across diverse species, including mouse and *Drosophila*[6,7], suggesting that this is an ancient CNS cell type. Curiously, evidence that zebrafish have bona fide astrocytes has, to date, been lacking[8,9]. Radial glial cells (RGCs), the precursor of astrocytes in mammals, have instead been proposed in zebrafish to functionally substitute for astrocytes. In zebrafish, RGCs serve as neural progenitor cells throughout life[10,11]; they typically exhibit bipolar shape with long processes spanning the entire parenchyma[9]; and recent studies argue that a subset indeed plays important roles in modulating zebrafish behavior[12].

Here we report the discovery and characterization of a cell type in the zebrafish CNS that is remarkably similar to mammalian astrocytes. By generating a stable transgenic line that labels the membrane and nuclei of all Glast$^+$ (glutamate aspartate transporter) cells, we found cells with dense cellular processes in both the brain and spinal cord of zebrafish larvae. Using a collection of new tools, we examined the cells with single-cell resolution and demonstrate that they elaborate a dense meshwork of fine cellular processes, morphologically similar to astrocytes in *Drosophila* and mammals. Time-lapse in vivo confocal microscopy showed that these cells begin to transform from RGCs into astrocyte-like cells at 2 d post-fertilization (dpf) in the spinal cord and display dynamic process elaboration over the course of development. These cells exhibit several additional defining characteristics of mammalian astrocytes, including expression of glutamine synthetase (GS), close association with synapses and astrocyte–astrocyte tiling behavior. By performing in vivo Ca^{2+} imaging, we found that these cells exhibit spontaneous microdomain Ca^{2+} transients in the fine processes[13,14] with dynamics similar to Ca^{2+} transients in awake behaving mice[15,16], and they respond to norepinephrine (NE) application[17–19]. To begin exploring the molecular basis of astrocyte morphogenesis and function in vertebrates, we developed a cell-specific CRISPR–Cas9 approach that allows rapid disruption of genes of interest in zebrafish astrocytes. Using this approach, we show that Fgf receptors (*fgfr3* and *fgfr4*) are required for astrocyte morphogenesis. Our work establishes zebrafish as a new model system to explore astrocyte development and function, including the first opportunity to live-image astrocyte morphogenesis from birth to maturity in vivo, and provides new insights into the molecular and cellular mechanisms regulating astrocyte development and growth.

Results

Slc1a3b/Glast-expressing cells display dense meshwork morphology in the zebrafish larval brain and spinal cord. With the aim of identifying astrocyte-like glia in zebrafish, we first performed a targeted whole-mount in situ hybridization screen at 6 dpf to examine the expression of marker genes known to be highly enriched in both human and mouse astrocytes[20,21]. We found that the glutamate transporters *slc1a2b* (*EAAT2a*/*GLT-1*) and *slc1a3b*

[1]Vollum Institute, Oregon Health & Science University, Portland, OR, USA. [2]Department of Biochemistry & Biophysics, University of California, San Francisco, San Francisco, CA, USA. [3]Kavli Institute for Fundamental Neuroscience, San Francisco, CA, USA. ✉e-mail: chenjia@ohsu.edu; monk@ohsu.edu

(*EAAT1b*/*Glast*) and GABA transporter *slc6a11b* (*GAT-3*) are expressed in the zebrafish larval CNS at 6 dpf (Extended Data Fig. 1a). We further characterized their expression patterns at different developmental stages and observed that all three of these genes could be detected at 1 dpf in restricted CNS regions (Extended Data Fig. 1b). At 3 dpf, they express more broadly in the CNS with some overlapping and unique expression patterns (Extended Data Fig. 1b), and brain expression was maintained through later larval stages (Extended Data Fig. 1c). To explore the nature of these potential astrocyte-like cells further, we generated a stable transgenic line, *Tg[slc1a3b:myrGFP-P2A-H2AmCherry]*, in which membrane-targeted myristoyl-GFP (myrGFP) and the nuclear marker H2AmCherry were expressed under the control of the *slc1a3b*/*Glast* promoter (Fig. 1a). We observed strong expression of myrGFP and H2AmCherry markers throughout the CNS in 6-dpf larvae (Fig. 1b) and a dense meshwork of myrGFP-labeled cellular processes in brain regions that likely house the synaptic neuropil[22] (Fig. 1c). In the spinal cord, we observed similar complex cellular processes in lateral regions (Fig. 1d–d"), the position of which overlap with the synapse-rich lateral neuropil. Given that astrocytes in flies and mammals intimately associate with synapses[7,23], we take the spatial organization of these fine membranes near CNS synapses as further support for the notion that these cells are astrocyte-like cells in zebrafish.

To enable analysis of these Glast$^+$ cells at single-cell resolution, we injected *slc1a3b:myrGFP-P2A-H2AmCherry* DNA constructs into one-celled zygotes to sparsely label individual cells. With this approach, we could identify RGCs that exhibit bipolar morphology as well as ependymal cells in the CNS ventricular zone (Extended Data Fig. 2). In zebrafish, recent dye-filling studies marked glial cells termed 'radial astrocytes' in the medulla oblongata with long processes that ramify at distal ends[12]. We first tested whether we could detect these cells in the hindbrain using our reporter construct. At 6 dpf, we found labeled cells in the hindbrain with nuclei at the midline and one main process extended laterally with bushy branches (Fig. 1e), similar to the previously reported radial astrocytes[12]. We noticed that *myrGFP* is highly expressed in the cerebellum in the transgenic line (Fig. 1c), consistent with the enrichment of Glast expression in mouse cerebellum[24]. By sparse labeling, we detected cells with somata sitting ventrally and extending a dense meshwork of processes toward the pial surface in the cerebellum at 6 dpf (Fig. 1f), which are similar to Bergmann glia, a specialized subset of astrocytes, in mammals[25]. We next analyzed the spinal cord with single-cell clones and found a cell type elaborating membrane projections with increasing density of fine processes laterally (Fig. 1g,g'). In contrast to the radial astrocytes that show thin long processes with bushy ends, these cells began to ramify complex processes in close proximity to their somata. Collectively, these data indicate that there are astrocyte-like cells in the zebrafish larval CNS, with morphology highly similar to astrocytes characterized in *Drosophila* and mammals. Hereafter, we refer to these cells as zebrafish spinal cord astrocytes.

Zebrafish spinal cord astrocytes dynamically elaborate processes and establish unique spatial domains at early larval stages. As mammalian astrocytes are derived from RGCs during postnatal development, we sought to test whether zebrafish astrocytes derive from RGCs in the spinal cord. Transparent zebrafish larvae offer the unique opportunity to live-image the morphogenesis of single RGCs and astrocytes from birth through late larval stages in vivo. At 1 dpf, clones sparsely labeled with *slc1a3b:myrGFP-P2A-H2AmCherry* had a radial glial-like morphology, with the nuclear marker H2AmCherry positioned close to the ventricular midline and a long main process extended toward the lateral pial surface. By time-lapse confocal imaging, we found that most of the analyzed cells at 1 dpf differentiated into neurons, consistent with the role of RGCs serving as neural progenitors during early neurogenesis[26]. The myrGFP/H2AmCherry markers subsequently diminished in the labeled neurons, likely owing to the silencing of *slc1a3b*/*Glast* promoter in the neural lineage. However, starting at 2 dpf, we observed individual cells exhibiting dynamic cellular process that became increasingly elaborate over developmental time toward the lateral synaptic neuropil regions of the spinal cord (Fig. 2a,d and Supplementary Video 1). We tracked the dynamics of astrocyte growth by repeatedly imaging individually labeled cells from 2 through 9 dpf in intact larvae ($n = 40$–59 individual cell clones; $n = 20$–25 fish analyzed at each stage). We quantified the spatial territory of individual cells and found that astrocytes in the developing spinal cord increased in size to rapidly establish their overall spatial domains between 2 and 4 dpf ($1{,}333 \pm 669.5\,\mu m^3$ at 2 dpf versus $2{,}629 \pm 813.7\,\mu m^3$ at 4 dpf; $P < 0.0001$, one-way analysis of variance (ANOVA) with Tukey's post hoc test) and then appeared to maintain individual territories thereafter (Fig. 2b,c). Astrocyte expansive growth is, therefore, most robust between 2 and 4 dpf, with subsequent growth not leading to significant expanded domain size (Fig. 2d) but perhaps elaboration of more intimate contacts with synapses, other glia and the vasculature during this later time window.

Spinal cord astrocytes express additional astrocyte markers, elaborate fine processes during synapse formation and tile with other astrocytes. We next sought to determine whether zebrafish astrocytes share additional cardinal features with mammalian astrocytes. Previous studies in mammals showed that GS is specifically enriched in astrocytes[27]. We, therefore, performed immunostaining experiments on *Tg[slc1a3b:myrGFP-P2A-H2AmCherry]* transgenic larvae with an anti-GS antibody. We found that GS was localized in the spinal cord cell somata as well as in the dense processes, which were co-labeled by the astrocytic myrGFP and H2AmCherry markers (Fig. 3a), suggesting that GS is present in these astrocytes. In addition, we compared the expression of *slc1a3b* with other common mammalian astrocyte markers, *gfap* and *kcnj10a*/*kir4.1*, by in situ hybridization experiments. We found that, in the 3-dpf spinal cord, expression of *slc1a3b* and *kcnj10a* were spatially restricted to the ventricular zone, and *kcnj10a* expression seemed to mostly overlap with myrGFP-labeled astrocytes in the spinal cord (Extended Data Fig. 3a,b). In contrast, we observed that *gfap* was expressed more broadly throughout the spinal cord compared to *slc1a3b* or *kcnj10a* (Extended Data Fig. 3a). Moreover, we detected diminished expression of *gfap* in 3-dpf larval brain regions, in contrast to the expression of *slc1a3b* (Extended Data Fig. 3a,c), suggesting spatiotemporally different regulation of these two genes across the CNS. Together, these data indicate that *slc1a3b*-labeled astrocytes also express *kcnj10a* and *gfap*, with *gfap* likely expressed in other cell types as well, which is consistent with recent single-cell RNA-sequencing studies in zebrafish[28].

In the developing and adult CNS, astrocyte processes enwrap synaptic structures and regulate synapse plasticity[23,29,30]. To determine whether zebrafish astrocytes also associate closely with synapses during development, we examined the spatiotemporal correlation between our transgenic markers and the presynaptic marker synaptic vesicle glycoprotein 2A (SV2). This was performed in the developing spinal cord at 2–4 dpf and 6 dpf, stages at which astrocyte morphologies are rapidly growing or relatively stable, respectively. We found that anti-SV2 staining in the spinal cord increased dramatically from 2 to 6 dpf, and this was highly correlated with the growth of astrocyte processes labeled by myrGFP (Fig. 3b). At 6 dpf, when we examined this relationship more closely with high-resolution microscopy, we found that myrGFP-labeled astrocyte processes were indeed in close apposition to SV2-labeled synaptic structures throughout the spinal cord (Fig. 3c). Taken together, these data indicate that astrocyte growth in the spinal cord is tightly associated with synapse formation in zebrafish, and

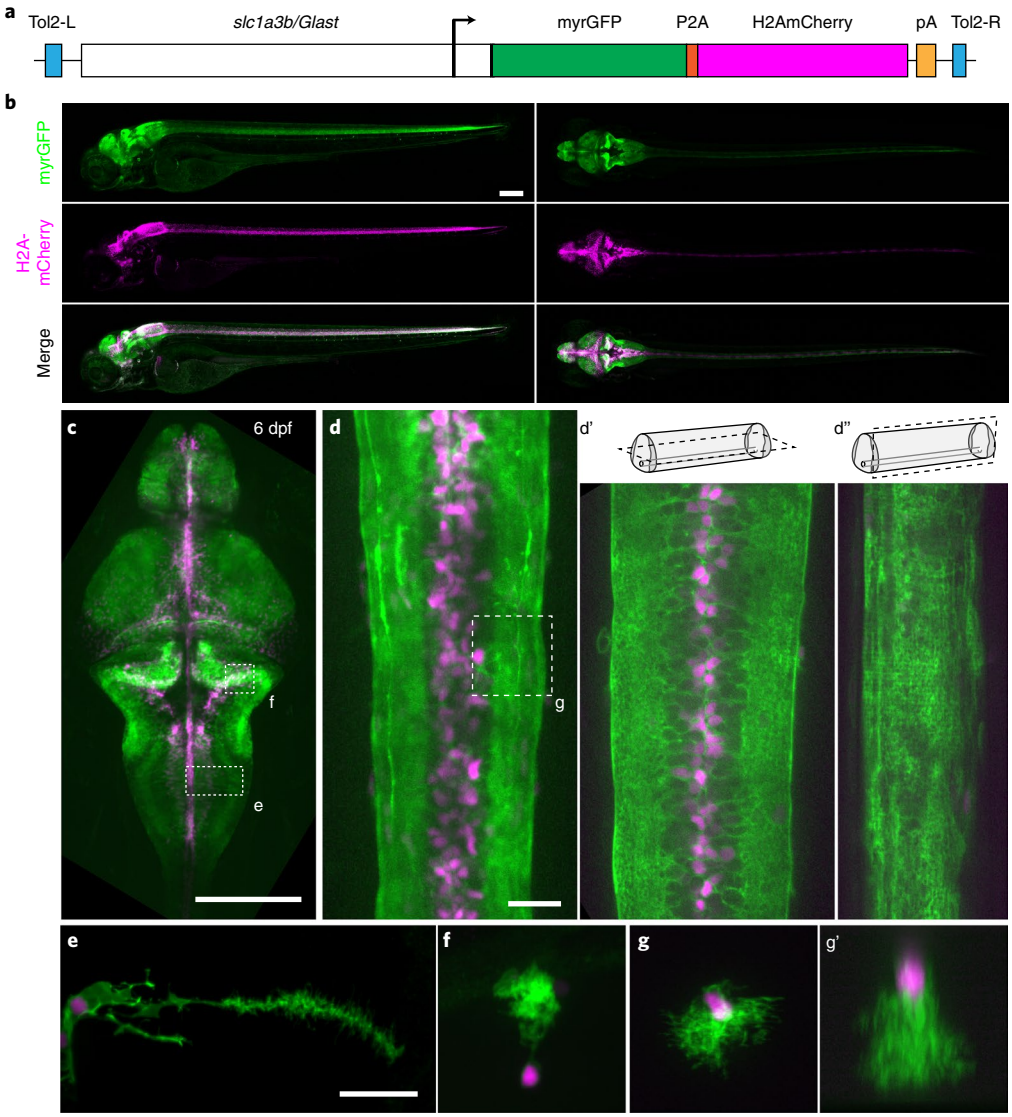

Fig. 1 | Slc1a3b/Glast$^+$ cells in zebrafish exhibit complex cellular morphologies. a, Schematic of the *slc1a3b:myrGFP-P2A-H2AmCherry* Tol2 DNA construct used for generating a stable transgenic line. **b**, MAX projection from the lateral and dorsal views of a representative *Tg[slc1a3b:myrGFP-P2A-H2AmCherry]* larva, showing the expression of myrGFP and H2AmCherry at 6 dpf. Scale bar, 200 µm. **c**, MAX projection of *Tg[slc1a3b:myrGFP-P2A-H2AmCherry]* larval brain at 6 dpf from the dorsal view. Small dashed boxes indicate the regions shown in **e** and **f**. Scale bar, 200 µm. **d**–**d″**, Representative images of Slc1a3b-expressing nuclear H2AmCherry and membrane myrGFP in a 6-dpf spinal cord. The small dashed box indicates the region shown in **g**. **d**, MAX projection; **d′**, a single *z* plane from the dorsal view; **d″**, a single *z* plane from the lateral view. Scale bar, 20 µm. **e**–**g′**, Mosaic labeling single-cell clones using an *slc1a3b:myrGFP-P2A-H2AmCherry* DNA construct in different CNS regions at 6 dpf. **e**, Posterior hindbrain (dorsal view). **f**, Cerebellum (lateral view). **g**, Spinal cord (lateral view). **g′**, Three-dimensional reconstruction of the spinal cord clone (**g**) from the dorsal view. Scale bar, 20 µm. Experiments in **b**–**d″** were independently repeated three or four times. **e**–**g′**, Representative images from $n=6$ (**e**), $n=3$ (**f**) and $n=5$ (**g**, **g′**) fish larvae.

astrocyte processes cover the entire synaptic neuropil. In the developing mammalian CNS, several studies have demonstrated that astrocyte-derived signals are important to promote synaptogenesis[29,31,32]. Thus, our data suggest that astrocyte processes need to be proximal to synaptic structures to fulfill their function, consistent with mammalian studies.

Mammalian astrocytes tile with one another to minimize overlap with other astrocytes and ensure full coverage of CNS neuropil[33]. To test whether zebrafish astrocytes exhibit tiling behavior, we injected two different membrane-labeled DNA constructs driven by the *slc1a3b/Glast* promoter (*slc1a3b:myrGFP* and *slc1a3b:mCD8mCherry*) into one-celled zygotes and looked for labeled neighboring clones that expressed either myrGFP or mCD8mCherry at 6 dpf. We found that, indeed, the *slc1a3b:myrGFP*-expressing clone is closely apposed to the *slc1a3b:mCD8mCherry*-expressing clone with limited overlap (Fig. 3d and Supplementary Video 2), suggesting that zebrafish astrocytes tile with each other and likely occupy unique territories.

Zebrafish astrocytes exhibit spontaneous microdomain Ca^{2+} transients and respond to NE. In the CNS, individual astrocytes interact with thousands of synapses; they also intimately contact neuronal cell bodies, blood vessels and other glial cells. Previous studies have argued that astrocytes can form functionally independent compartments that adapt to local demands and exhibit spontaneous microdomain Ca^{2+} activities[15]. To determine whether zebrafish astrocytes are capable of increasing Ca^{2+} transients locally in the fine processes, and the dynamics of such

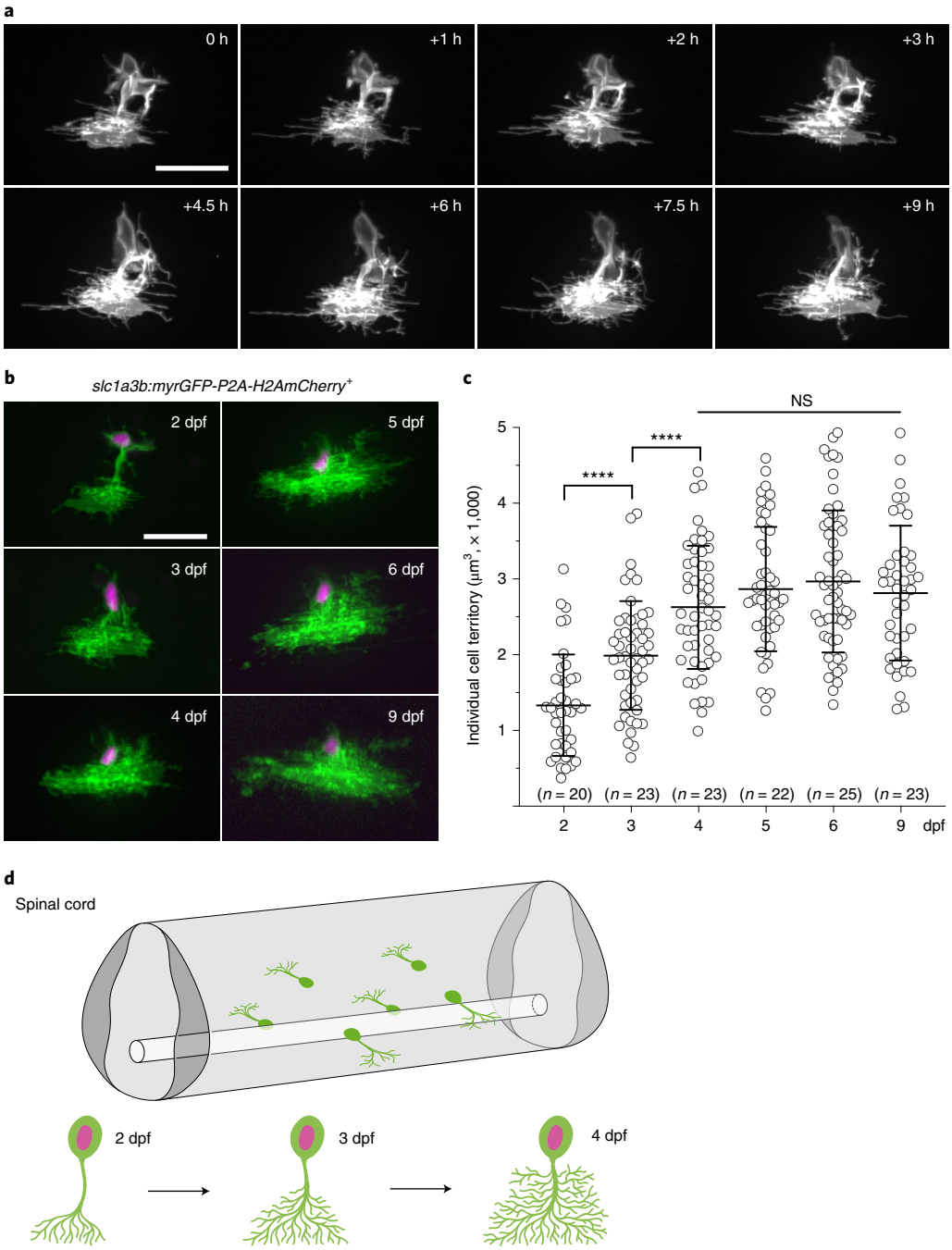

Fig. 2 | Zebrafish spinal cord astrocytes show dynamic cellular process elaboration and establish individual cell territories between 2 and 4 dpf. a, Time-lapse still images of an *slc1a3b:myrGFP-P2A-H2AmCherry*-expressing astrocyte in the spinal cord between 2 and 3 dpf. Scale bar, 20 μm. See also Supplementary Video 1. **b**, Representative images show the same astrocyte at different developmental stages in the spinal cord. MAX projection, lateral view. Scale bar, 20 μm. **c**, Quantification of individual spinal cord astrocyte cell territory between 2 and 9 dpf. ****$P < 0.0001$; NS, not significant; one-way ANOVA with Tukey's post hoc test. *n*, number of fish analyzed. Error bars represent mean values ± s.d. **d**, Schematic showing the developmental stages important for spinal cord astrocyte growth.

events, we generated a transgenic line, *Tg[slc1a3b:myrGCaMP6s]*, in which a membrane-targeted myristol-Ca^{2+} indicator GCaMP6s (myrGCaMP6s) is expressed under the control of the *slc1a3b/Glast* promoter. By performing time-lapse confocal imaging with this transgenic line at 6 dpf in the larval spinal cord, we observed robust microdomain Ca^{2+} transients in astrocyte fine processes (Fig. 4a and Supplementary Video 3). We analyzed the Ca^{2+} events with automated Astrocyte Quantitative Analysis (AQuA) software[34] (Fig. 4a–c) and found that microdomain Ca^{2+} events exhibit diverse ranges of activities: individual events vary in domain area size, amplitude and duration (Fig. 4d–f; $n = 1{,}239$ events, $n = 6$ fish analyzed). On average, these events have slow kinetics (5.84 ± 3.81 s), similar to those found in mouse astrocytes[34–36].

In mammals, a startle stimulus or direct application of NE has been shown to promote microdomain Ca^{2+} events[37]. To test whether zebrafish astrocytes are sensitive to NE signaling, we performed live Ca^{2+} imaging in the intact larval spinal cord with the treatment of NE or dimethylsulfoxide (DMSO) control at 6 dpf (Supplementary

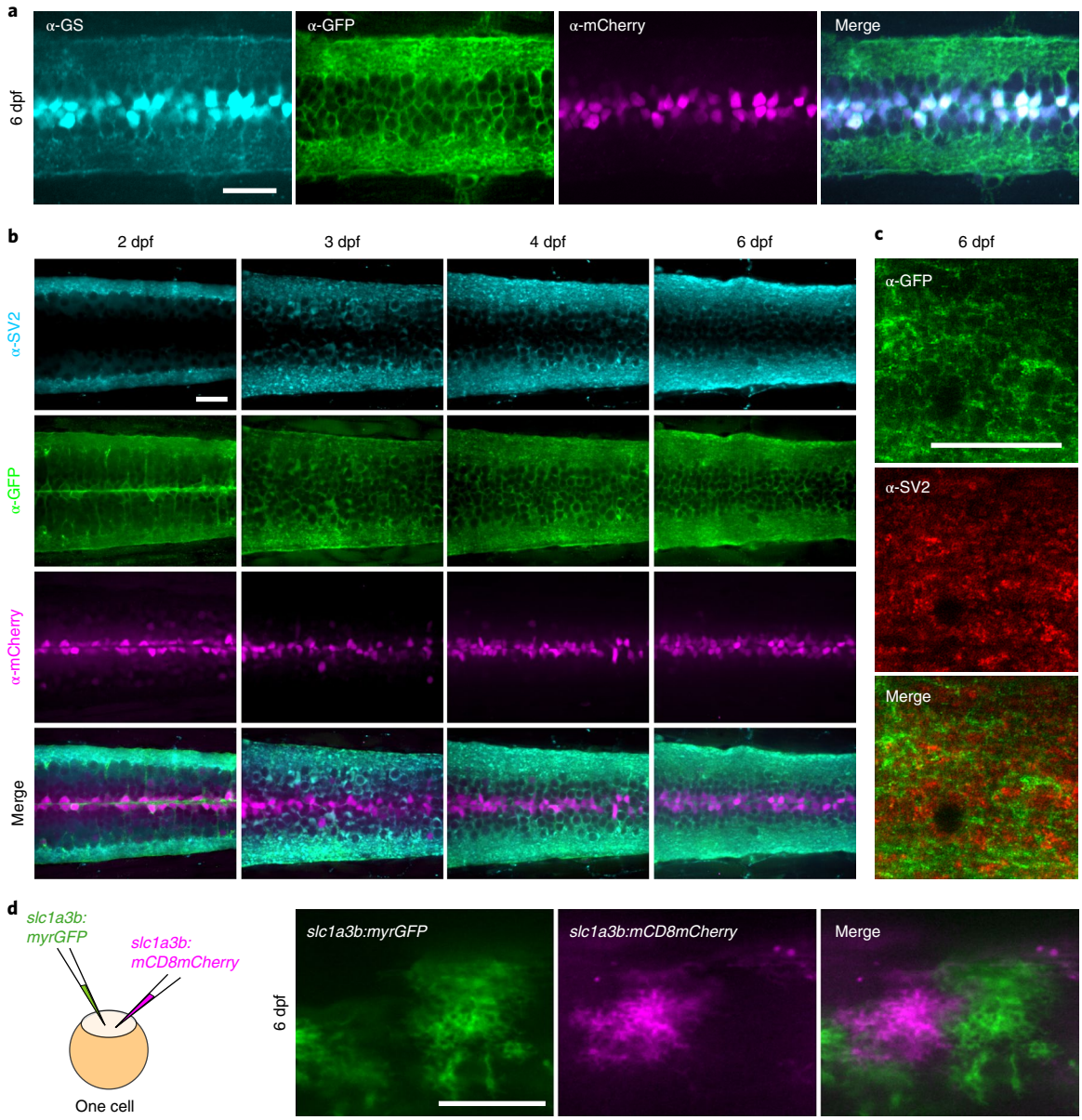

Fig. 3 | Spinal cord astrocytes express GS, closely associate with synapses and tile with one another. a, Immunostaining of GS in *Tg[slc1a3b:myrGFP-P2A-H2AmCherry]* fish spinal cord at 6 dpf. Single *z* plane, dorsal view. Representative images from $n=8$ fish larvae. **b**, Immunostaining of SV2 in *Tg[slc1a3b:myrGFP-P2A-H2AmCherry]* fish spinal cord at 2–6 dpf. Single *z* plane, dorsal view. Representative images from $n=7$ fish larvae. **c**, Higher-resolution imaging shows the close apposition of myrGFP-labeled astrocyte membranes with synapses (α-SV2, red) in the spinal cord neuropil at 6 dpf (lateral view). Scale bar, 20 µm. Representative images from four independent repeats. **d**, Representative images show two tiling astrocytes labeled with *slc1a3b:myrGFP* (green) and *slc1a3b:mCD8mCherry* (red) in the 6-dpf larval spinal cord. Cartoon depicts how the experiments were performed to produce two individually labeled cells. Scale bar, 20 µm. Representative images from $n=5$ fish larvae. See also Supplementary Video 2.

Videos 4 and 5) (DMSO, $n=8$ fish; NE, $n=9$ fish). Using AQuA for quantification, we found a significant increase in microdomain Ca^{2+} events in NE-treated spinal cord astrocytes compared to DMSO controls (DMSO, 4.68 ± 1.47 events per minute; NE, 18.80 ± 3.39 events per minute in normalized 1,000 µm^2 area; $P=0.0023$, two-tailed unpaired *t*-test) (Fig. 4g,h). The average duration of Ca^{2+} transients was increased in NE-treated astrocytes (DMSO, 5.46 ± 4.21 s; NE, 7.42 ± 5.69 s; $P<0.0001$, two-tailed unpaired *t*-test) (Fig. 4i–k), whereas the average microdomain area appeared unaltered (DMSO, 7.81 ± 0.65 µm^2; NE, 6.81 ± 0.24 µm^2; $P=0.0837$, two-tailed unpaired *t*-test), and the average amplitude was slightly decreased (DMSO, 0.39 ± 0.08 $\Delta F/F$; NE, 0.34 ± 0.09 $\Delta F/F$; $P<0.0001$, two-tailed unpaired *t*-test). To test whether the response of spinal cord astrocytes to NE signaling requires neuronal activity, we injected tetrodotoxin (TTX) into the yolk of 6-dpf *Tg[slc1a3b:myrGCaMP6s]* larvae to block voltage-gated sodium channels[38]. This injection paralyzed the larvae, indicating the efficacy of TTX administration, and injected larvae were treated with NE or DMSO before Ca^{2+} imaging (Extended Data Fig. 4a). We found that TTX treatment had no effect on the increased number of NE-induced microdomain Ca^{2+} events in spinal cord astrocytes (TTX + DMSO, 5.31 ± 0.88 events per minute; TTX + NE, 14.01 ± 2.86 events per minute in normalized 1,000 µm^2 area; $P=0.0094$, two-tailed unpaired *t*-test) or the increased duration of Ca^{2+} transients in NE-treated astrocytes (TTX + DMSO, 5.15 ± 4.11 s; TTX + NE, 7.62 ± 6.97 s; $P<0.0001$, two-tailed unpaired *t*-test) (Extended Data Fig. 4b,c)

($n=10$ fish for each group). However, the average microdomain area was reduced (TTX + DMSO, $7.81 \pm 0.64\,\mu m^2$; TTX + NE, $4.83 \pm 0.24\,\mu m^2$; $P<0.0001$, two-tailed unpaired *t*-test), and the average amplitude was increased (TTX + DMSO, $0.24 \pm 0.08\ \Delta F/F$; TTX + NE, $0.30 \pm 0.08\ \Delta F/F$; $P<0.0001$, two-tailed unpaired *t*-test) in NE-treated astrocytes after TTX injection (Extended Data Fig. 4d,e). Together, these data show that neuronal activity is dispensable for NE-induced astrocyte microdomain Ca^{2+} frequency and duration but might play a role in influencing Ca^{2+} microdomain size and amplitude.

As a recent study demonstrated that radial astrocytes in zebrafish hindbrain can respond to NE activation to elicit cytosolic Ca^{2+} events[12], we also performed Ca^{2+} imaging experiments in the hindbrain region to test whether microdomain Ca^{2+} activity can be influenced in radial astrocytes by NE signaling. Consistent with our data in the spinal cord, we observed a similar increase in NE-induced microdomain Ca^{2+} events in the hindbrain radial astrocyte fine processes (Extended Data Fig. 5 and Supplementary Videos 6 and 7) (DMSO, $n=8$ fish; NE, $n=8$ fish). Together, these results show that zebrafish astrocytes exhibit Ca^{2+} signaling dynamics that are remarkably similar to those in awake behaving mice, and that, as in mice, NE promotes microdomain Ca^{2+} events in zebrafish astrocytes by increasing the total number of microdomain events and enhancing the duration of individual events.

A cell-specific CRISPR–Cas9 approach to study astrocyte gene function in vivo. Our data indicate that zebrafish have astrocytes that are morphologically, molecularly and functionally similar to mammalian astrocytes. Given that little is still known about astrocyte development and function in vivo, we aimed to develop a rapid assay in zebrafish to genetically manipulate candidate genes in an astrocyte-specific manner. To this end, we adapted a tissue-specific CRISPR–Cas9 system[39] along with the sparse labeling approach to inactivate genes and assay their function in individual astrocyte clones in the F_0 generation. Briefly, we generated a DNA construct (*slc1a3b:Cas9*;*U6:sgRNA*) to express *sgRNAs* ubiquitously while driving Cas9 expression under the *slc1a3b/Glast* promoter. We co-injected our *slc1a3b:myrGFP-P2A-H2AmCherry* reporter constructs together with *slc1a3b:Cas9*;*U6:sgRNA* DNA to target genes of interest into zygotes and carried out mosaic analyses of myrGFP/H2AmCherry-labeled cells in the injected F_0 larvae (Fig. 5a). Owing to the high efficacy of CRISPR–Cas9 in zebrafish, gene function can routinely be studied in the F_0 generation[40].

As a proof of principle, we decided to test whether Fgf receptors play a role in astrocyte morphogenesis in zebrafish. In *Drosophila*, astrocyte depletion of Fgf receptor Heartless (Htl) has been shown to lead to strong defects in astrocyte morphogenesis in the developing CNS[7]. We sought to test whether the function of Fgf signaling is conserved in vertebrate astrocyte development. In zebrafish, there are five homologous genes encoding *fgf* receptors: *fgfr1a*, *fgfr1b*, *fgfr2*, *fgfr3* and *fgfr4*. We first validated the efficiency of *sgRNAs* by injecting synthetic *sgRNAs* targeting individual *fgfr* genes together with Cas9 protein into early zygotes and performed genotyping polymerase chain reaction (PCR) at 1 dpf to examine targeted mutation efficiency. The designed *sgRNAs* displayed high efficiency in disrupting targeted loci (Extended Data Fig. 6), underscoring the likelihood of frameshift mutation generation in corresponding genes. We next performed mosaic clonal analyses of individual *fgfr* gene-targeted cells in the spinal cord at 6 dpf ($n=34$–98 individual clones examined and $n=10$–37 fish examined). When injecting empty vector-based control *sgRNA* DNA, more than 90% of the clones exhibited normal morphology (Class I) with dense elaborated processes in the neuropil (Fig. 5b). In contrast, in *fgfr sgRNA*-targeted astrocytes, we found that *fgfr1a*, *fgfr1b* and *fgfr2* were dispensable, but *fgfr3* and *fgfr4* were required for astrocytic process elaboration (Fig. 5b), Specifically, at 6 dpf, we found that ~60% of myrGFP-labeled clones (Class II, 39.8%; Class III, 18.4%) exhibited aberrant process elaboration phenotypes upon astrocyte-specific disruption of *fgfr3* (Fig. 5b), and individual *fgfr3*-inactivated astrocytes showed decreased cell volume compared to controls (control, $3{,}617 \pm 1{,}440\,\mu m^3$; *fgfr3*, $2{,}807 \pm 1{,}543\,\mu m^3$; $P=0.0131$, two-tailed unpaired *t*-test) (Fig. 5c,d). Similarly, 39% of *fgfr4*-targeted cells showed abnormal morphology in the spinal cord (Class II, 26.5%; Class III, 12.2%) (Fig. 5b) and displayed reduced cell volume as well (*fgfr4*, $2{,}854 \pm 979\,\mu m^3$, $P=0.0379$, two-tailed unpaired *t*-test) (Fig. 5c,d). In addition, we found that other myrGFP-labeled cells, such as RGCs and ependymal cells, appeared grossly normal when *fgfr3* and *fgfr4* were inactivated (RGCs, $n=10/10$ normal clones; ependymal cells, $n=33/35$ normal clones). Thus, these data suggest that Fgf receptors play a conserved role in vertebrate astrocyte growth, and that the cell-specific CRISPR–Cas9 approach we developed here works efficiently to uncover astrocyte gene function.

Discussion

Zebrafish represent an excellent vertebrate model system to study neurodevelopment in vivo. The transparency of zebrafish embryos and young larvae makes them accessible to long-term cell fate tracing in intact animals and to imaging of molecular and cellular behaviors by time-lapse microscopy, but bona fide astrocytes have not been identified in this model system. Here we report a previously undescribed glial cell type in zebrafish with several defining characteristics of mammalian astrocytes, including their intricate bushy morphology, expression of astrocyte markers Glast and GS, close association with synapses, tiling behavior and dynamic global and microdomain Ca^{2+} transients. Most of the growth of these cells occurs during 2–4 dpf in the spinal cord, and, using a cell-specific CRISPR–Cas9 approach, we demonstrated that *fgfr3* and *fgfr4* are required in spinal cord astrocytes for proper morphogenesis. This work establishes zebrafish as a powerful new model to study astrocytes, which should allow for rapid forward genetic screening to identify novel genes critical for many aspects of astrocyte development and function.

In mammals, astrocytes are derived from RGCs, which serve as neural progenitors during early brain development[41]. By late neurogenesis, most RGCs retract their cell bodies from the ventricles and become stellate-like astrocytes[42]. Similarly, in zebrafish, RGCs have been characterized in various CNS regions during development[26,43]. However, in contrast to mammals, zebrafish RGCs persist in most regions of the adult CNS and are thought to be responsible for the impressive CNS regenerative capacity observed in this species[10,44].

Fig. 4 | Zebrafish astrocytes exhibit spontaneous microdomain Ca^{2+} transients in the fine processes and respond to NE activation. a, Representative image showing 5-min time overlay of Ca^{2+} events in a single *z* plane in *Tg[slc1a3b:myrGCaMP6s]* fish cellular process-enriched lateral region (lateral view) at 6 dpf. Scale bar, 20 µm. See also Supplementary Video 3. **b**, AQuA-detected Ca^{2+} events, with individual events pseudo-colored. **c**, Representative $\Delta F/F$ traces of 20 individual microdomain Ca^{2+} transients. **d**–**f**, Quantifications of astrocyte microdomain Ca^{2+} event area size (**d**), amplitude (**e**) and duration (**f**) in the spinal cord. Error bars represent mean values ± s.e.m. **g**, AQuA-detected Ca^{2+} events in DMSO control versus NE-treated *Tg[slc1a3b:myrGCaMP6s]* fish spinal cord astrocytes and corresponding 20 individual $\Delta F/F$ traces during 5 min. Scale bar, 20 µm. See also Supplementary Videos 4 and 5. **h**–**k**, Comparisons of average microdomain Ca^{2+} events frequencies (**h**), area sizes (**i**), amplitudes (**j**) and durations (**k**) in DMSO control and NE-treated fish. Error bars represent mean values ± s.d. $^{**}P<0.01$; NS, not significant; $^{****}P<0.0001$. $P=0.0023$ (**h**); $P=0.0837$ (**i**); $P<1.0\times10^{-15}$ for **j** and **k**. Two-tailed unpaired *t*-test. *n*, number of fish analyzed.

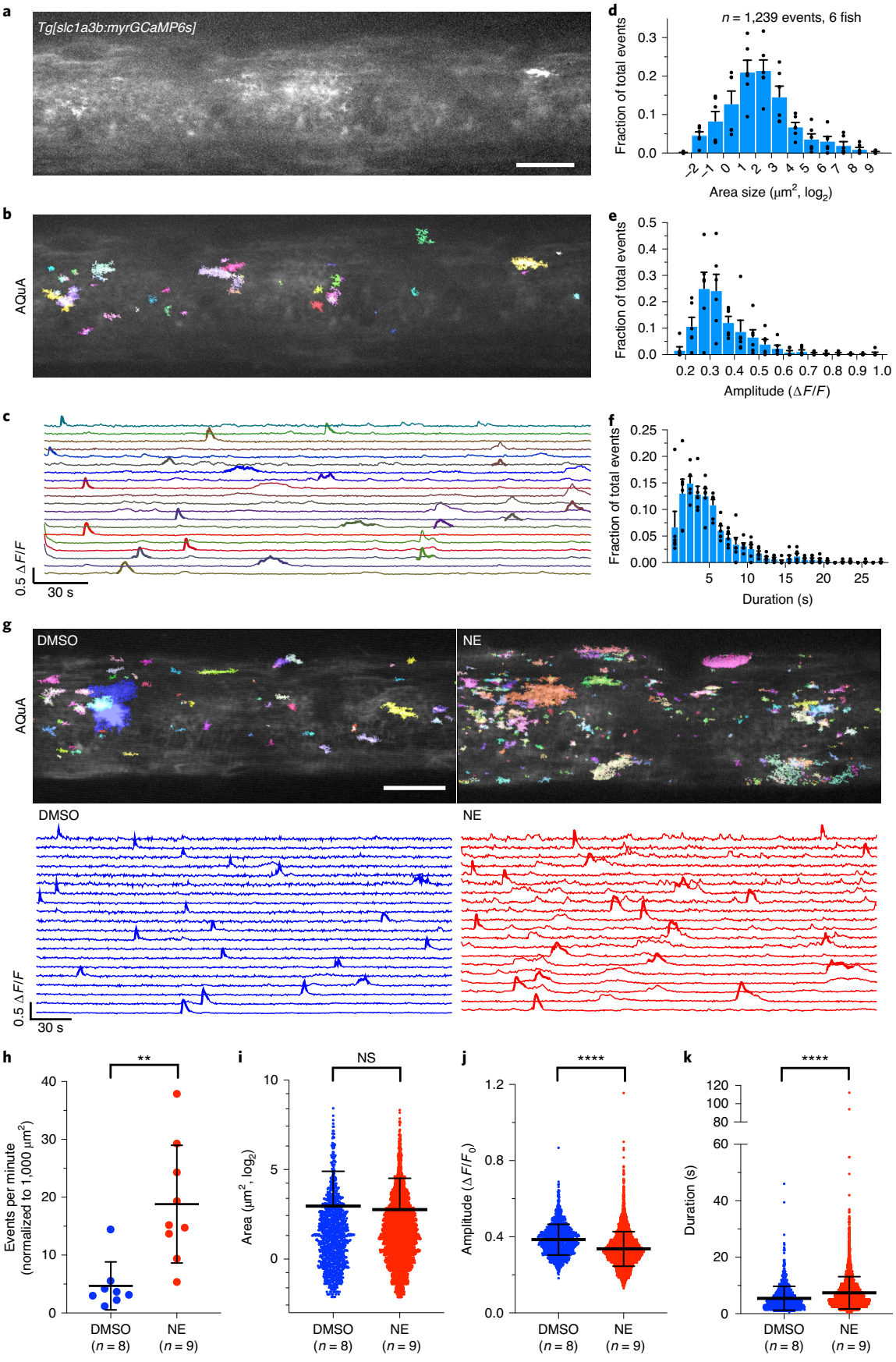
a
Tg[slc1a3b:myrGCaMP6s]
b
AQuA
c
0.5 ΔF/F
30 s
d
n = 1,239 events, 6 fish
Fraction of total events
Area size (μm², log2)
e
Fraction of total events
Amplitude (ΔF/F)
f
Fraction of total events
Duration (s)
g
DMSO
NE
AQuA
DMSO
NE
0.5 ΔF/F
30 s
h
Events per minute (normalized to 1,000 μm²)
DMSO (n = 8)
NE (n = 9)
i
NS
Area (μm², log2)
DMSO (n = 8)
NE (n = 9)
j
****
Amplitude (ΔF/F0)
DMSO (n = 8)
NE (n = 9)
k
****
Duration (s)
DMSO (n = 8)
NE (n = 9)

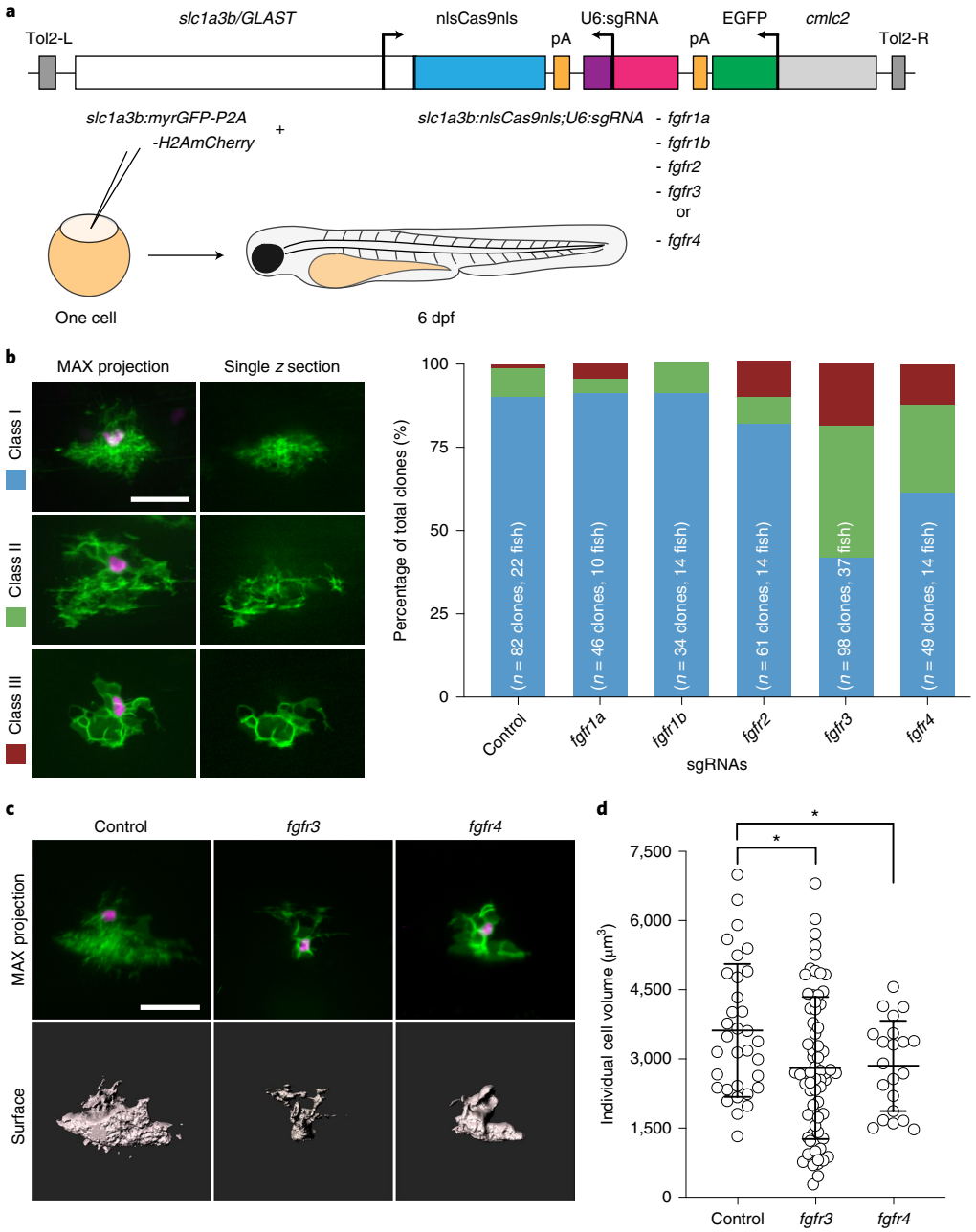

Fig. 5 | Cell-specific inactivation of *fgfr3* and *fgfr4* disturbs spinal cord astrocyte morphogenesis. a, Schematic of the *slc1a3b:nlsCas9nls;U6-sgRNA* DNA construct used for gene inactivation and the experimental design. **b**, Representative images showing the three main classes of labeled clones observed at 6 dpf after injections and the quantifications of each *fgfr* gene-inactivated cell in comparison with the control *sgRNA* group. Scale bar, 20 μm. **c**, Representative images and Imaris-generated three-dimensional models of control, *fgfr3* and *fgfr4*-disrupted astrocytes. Scale bar, 20 μm. **d**, Quantification of individual astrocyte volumes in control, *fgfr3* and *fgfr4*-disrupted cells in the 6-dpf spinal cord. Error bars represent mean values ± s.d. Control, $n = 33$ cells in 18 fish analyzed; *fgfr3*, $n = 68$ cells in 33 fish analyzed; *fgfr4*, $n = 21$ cells in 12 fish analyzed. $^*P < 0.05$. For control versus *fgfr3*, $P = 0.0131$; for control versus *fgfr4*, $P = 0.0379$. Two-tailed unpaired *t*-test.

It has remained controversial whether zebrafish have true astrocytes that have not yet been described or if zebrafish RGCs might perform necessary functions of astrocytes. Our work demonstrates that the zebrafish CNS indeed houses a population of astrocytes very similar to those in mammals and *Drosophila*. This provides further support for the notion that astrocytes are an ancient, well-conserved CNS cell type. We also noted that spinal cord astrocytes and radial astrocytes in the hindbrain exhibit morphological differences, with hindbrain radial astrocytes maintaining a long main process between the cell body and the dense branches. However, given the similarities in molecular markers and responses to NE signaling, it is possible that spinal cord astrocytes and hindbrain radial astrocytes represent a same cell type or closely related cell types in different CNS areas, whereby surrounding cells or structural constraints might play a role in regulating their morphogenesis. In the zebrafish spinal cord, using several new markers, we were able to live-image astrocyte morphogenesis from birth through late larval stages as they establish their unique spatial domains. We found that

astrocytes show dynamic extension and retraction of cellular processes, rapidly occupy their final spatial domains and elaborate fine processes concomitant to the onset of synapse formation.

Understanding how astrocytes elaborate their remarkable morphologies, and how much of this process is guided intrinsically versus extrinsically, will be essential to understand their functions. Many of the key proposed functions for astrocytes require specialized cell–cell associations, such as endfeet on the vasculature or associations with synaptic elements. In mammals, the intimate association of astrocytes with neuropil is critical for synaptogenesis during development[23,29,31,32,45] and also later in mature circuits for neurotransmitter clearance and modulation of synaptic activity[30,46]. Although the precise roles for astrocyte Ca^{2+} signaling remain a point of controversy, microdomain Ca^{2+} transients have been implicated in local neural circuit control in multiple species[12,15]. Here we showed that zebrafish astrocyte Ca^{2+} transients are enhanced by NE stimulation (Fig. 4 and Extended Data Figs. 4 and 5). Our data, therefore, strongly suggest that zebrafish astrocytes function similarly to mammalian astrocytes with respect to Ca^{2+} signaling dynamics. Given the genetic tractability of zebrafish, along with our ability to live-image signaling in intact animals, a deep analysis of the mechanistic basis of Ca^{2+} signaling in zebrafish neural circuit function should provide exciting new insights into their function.

Little is understood about the signaling pathways that drive astrocyte morphogenesis and association with other CNS cell types. We have shown that astrocytes are derived from RGCs in the zebrafish spinal cord and, over 2–4 d, expand to occupy their unique spatial domains and then tile with one another (Fig. 2 and Supplementary Video 1). By developing a cell-specific CRISPR–Cas9 approach, we discovered that inactivating *fgfr3* and *fgfr4* in astrocytes abolished normal process infiltration in zebrafish (Fig. 5). In *Drosophila*, the *fgfr* homolog *htl* is critical for astrocyte growth and interaction of astrocyte processes with synapse-rich neuropil. Htl loss resulted in astrocytes with a similar less-intricate morphology that failed to elaborate fine processes in the synaptic neuropil[7]. In mammals, Fgf signaling has been shown to play a role in neural progenitors to switch cell fate from neurons to astrocytes[47]. In addition, *Fgfr3* has been found to be highly expressed in both human and mouse astrocytes[20,21,48]. However, whether Fgf signaling plays a role and which Fgf receptors (Fgfr1–4) are responsible for astrocyte morphogenesis in vertebrates remain unclear. Our data support the notion that Fgf signaling is a conserved feature of astrocyte morphogenesis in vertebrates and particularly of Fgfr3 and Fgfr4 in the spinal cord.

Astrocytes are integral components of neural circuits, modulating neuronal function in a variety of ways, but we still lack basic knowledge of astrocyte development and function in vivo. Studying astrocyte biology in vivo is crucial, as astrocytes radically transform their phenotypes when placed in cell culture. This work establishes zebrafish as a new system in which to explore astrocyte biology. Zebrafish astrocytes develop over the course of only a few days; one can exploit the battery of genetic tools available in zebrafish to explore gene function; and imaging and manipulation can be performed with single-cell resolution, through the entirety of astrocyte development. As whole-brain imaging is becoming quite common in zebrafish, even in animals executing simple behaviors, our work lays the foundation for future studies to link specific changes in astrocyte signaling with changes in neural circuit function or behavior.

Online content

Any methods, additional references, Nature Research reporting summaries, source data, extended data, supplementary information, acknowledgements, peer review information; details of author contributions and competing interests; and statements of data and code availability are available at https://doi.org/10.1038/s41593-020-0703-x.

Received: 24 January 2020; Accepted: 24 July 2020;
Published online: 7 September 2020

References

1. Freeman, M. R. Specification and morphogenesis of astrocytes. *Science* **330**, 774–778 (2010).
2. Clarke, L. E. & Barres, B. A. Emerging roles of astrocytes in neural circuit development. *Nat. Rev. Neurosci.* **14**, 311–321 (2013).
3. Ma, Z., Stork, T., Bergles, D. E. & Freeman, M. R. Neuromodulators signal through astrocytes to alter neural circuit activity and behaviour. *Nature* **539**, 428–432 (2016).
4. Nagai, J. et al. Hyperactivity with disrupted attention by activation of an astrocyte synaptogenic cue. *Cell* **177**, 1280–1292 (2019).
5. Molofsky, A. V. et al. Astrocytes and disease: a neurodevelopmental perspective. *Genes Dev.* **26**, 891–907 (2012).
6. Freeman, M. R. & Rowitch, D. H. Evolving concepts of gliogenesis: a look way back and ahead to the next 25 years. *Neuron* **80**, 613–623 (2013).
7. Stork, T., Sheehan, A., Tasdemir-Yilmaz, O. E. & Freeman, M. R. Neuron-glia interactions through the Heartless FGF receptor signaling pathway mediate morphogenesis of *Drosophila* astrocytes. *Neuron* **83**, 388–403 (2014).
8. Lyons, D. A. & Talbot, W. S. Glial cell development and function in zebrafish. *Cold Spring Harb. Perspect. Biol.* **7**, a020586 (2014).
9. Grupp, L., Wolburg, H. & Mack, A. F. Astroglial structures in the zebrafish brain. *J. Comp. Neurol.* **518**, 4277–4287 (2010).
10. Kroehne, V., Freudenreich, D., Hans, S., Kaslin, J. & Brand, M. Regeneration of the adult zebrafish brain from neurogenic radial glia-type progenitors. *Development* **138**, 4831–4841 (2011).
11. Kyritsis, N. et al. Acute inflammation initiates the regenerative response in the adult zebrafish brain. *Science* **338**, 1353–1356 (2012).
12. Mu, Y. et al. Glia accumulate evidence that actions are futile and suppress unsuccessful behavior. *Cell* **178**, 27–43 (2019).
13. Di Castro, M. A. et al. Local Ca^{2+} detection and modulation of synaptic release by astrocytes. *Nat. Neurosci.* **14**, 1276–1284 (2011).
14. Shigetomi, E., Tong, X., Kwan, K. Y., Corey, D. P. & Khakh, B. S. TRPA1 channels regulate astrocyte resting calcium and inhibitory synapse efficacy through GAT-3. *Nat. Neurosci.* **15**, 70–80 (2011).
15. Grosche, J. et al. Microdomains for neuron-glia interaction: parallel fiber signaling to Bergmann glial cells. *Nat. Neurosci.* **2**, 139–143 (1999).
16. Nimmerjahn, A., Mukamel, E. A. & Schnitzer, M. J. Motor behavior activates Bergmann glial networks. *Neuron* **62**, 400–412 (2009).
17. Ding, F. et al. α1-Adrenergic receptors mediate coordinated $Ca2^{+}$ signaling of cortical astrocytes in awake, behaving mice. *Cell Calcium* **54**, 387–394 (2013).
18. Paukert, M. et al. Norepinephrine controls astroglial responsiveness to local circuit activity. *Neuron* **82**, 1263–1270 (2014).
19. Pankratov, Y. & Lalo, U. Role for astroglial α1-adrenoreceptors in gliotransmission and control of synaptic plasticity in the neocortex. *Front. Cell Neurosci.* **9**, 230 (2015).
20. Cahoy, J. D. et al. A transcriptome database for astrocytes, neurons, and oligodendrocytes: a new resource for understanding brain development and function. *J. Neurosci.* **28**, 264–278 (2008).
21. Zhang, Y. et al. An RNA-sequencing transcriptome and splicing database of glia, neurons, and vascular cells of the cerebral cortex. *J. Neurosci.* **34**, 11929–11947 (2014).
22. Turner, K. J., Bracewell, T. G. & Hawkins, T. A. Anatomical dissection of zebrafish brain development. *Methods Mol. Biol.* **1082**, 197–214 (2014).
23. Stogsdill, J. A. et al. Astrocytic neuroligins control astrocyte morphogenesis and synaptogenesis. *Nature* **551**, 192–197 (2017).
24. Regan, M. R. et al. Variations in promoter activity reveal a differential expression and physiology of glutamate transporters by glia in the developing and mature CNS. *J. Neurosci.* **27**, 6607–6619 (2007).
25. Bellamy, T. C. Interactions between Purkinje neurones and Bergmann glia. *Cerebellum* **5**, 116–126 (2006).
26. Lyons, D. A., Guy, A. T. & Clarke, J. D. Monitoring neural progenitor fate through multiple rounds of division in an intact vertebrate brain. *Development* **130**, 3427–3436 (2003).
27. Norenberg, M. D. & Martinez-Hernandez, A. Fine structural localization of glutamine synthetase in astrocytes of rat brain. *Brain Res.* **161**, 303–310 (1979).
28. Farnsworth, D. R., Saunders, L. M. & Miller, A. C. A single-cell transcriptome atlas for zebrafish development. *Dev. Biol.* **459**, 100–108 (2020).
29. Christopherson, K. S. et al. Thrombospondins are astrocyte-secreted proteins that promote CNS synaptogenesis. *Cell* **120**, 421–433 (2005).
30. Bernardinelli, Y. et al. Activity-dependent structural plasticity of perisynaptic astrocytic domains promotes excitatory synapse stability. *Curr. Biol.* **24**, 1679–1688 (2014).
31. Kucukdereli, H. et al. Control of excitatory CNS synaptogenesis by astrocyte-secreted proteins Hevin and SPARC. *Proc. Natl Acad. Sci. USA* **108**, E440–E449 (2011).

32. Allen, N. J. et al. Astrocyte glypicans 4 and 6 promote formation of excitatory synapses via GluA1 AMPA receptors. *Nature* **486**, 410–414 (2012).
33. Bushong, E. A., Martone, M. E., Jones, Y. Z. & Ellisman, M. H. Protoplasmic astrocytes in CA1 stratum radiatum occupy separate anatomical domains. *J. Neurosci.* **22**, 183–192 (2002).
34. Wang, Y. et al. Accurate quantification of astrocyte and neurotransmitter fluorescence dynamics for single-cell and population-level physiology. *Nat. Neurosci.* **22**, 1936–1944 (2019).
35. Nett, W. J., Oloff, S. H. & McCarthy, K. D. Hippocampal astrocytes in situ exhibit calcium oscillations that occur independent of neuronal activity. *J. Neurophysiol.* **87**, 528–537 (2002).
36. Araque, A. et al. Gliotransmitters travel in time and space. *Neuron* **81**, 728–739 (2014).
37. Agarwal, A. et al. Transient opening of the mitochondrial permeability transition pore induces microdomain calcium transients in astrocyte processes. *Neuron* **93**, 587–605 e587 (2017).
38. Kegel, L. et al. Disruption to NKCC1 impairs the response of myelinating Schwann cells to neuronal activity and leads to severe peripheral nerve pathology. Preprint at *bioRxiv* https://www.biorxiv.org/content/10.1101/757831v1.full (2019).
39. Ablain, J., Durand, E. M., Yang, S., Zhou, Y. & Zon, L. I. A CRISPR/Cas9 vector system for tissue-specific gene disruption in zebrafish. *Dev. Cell* **32**, 756–764 (2015).
40. Shah, A. N., Davey, C. F., Whitebirch, A. C., Miller, A. C. & Moens, C. B. Rapid reverse genetic screening using CRISPR in zebrafish. *Nat. Methods* **12**, 535–540 (2015).
41. Rowitch, D. H. & Kriegstein, A. R. Developmental genetics of vertebrate glial-cell specification. *Nature* **468**, 214–222 (2010).
42. Kriegstein, A. & Alvarez-Buylla, A. The glial nature of embryonic and adult neural stem cells. *Annu. Rev. Neurosci.* **32**, 149–184 (2009).
43. Johnson, K. et al. Gfap-positive radial glial cells are an essential progenitor population for later-born neurons and glia in the zebrafish spinal cord. *Glia* **64**, 1170–1189 (2016).
44. Goldshmit, Y. et al. Fgf-dependent glial cell bridges facilitate spinal cord regeneration in zebrafish. *J. Neurosci.* **32**, 7477–7492 (2012).
45. Eroglu, C. et al. Gabapentin receptor α2Δ-1 is a neuronal thrombospondin receptor responsible for excitatory CNS synaptogenesis. *Cell* **139**, 380–392 (2009).
46. Zhou, Y. & Danbolt, N. C. GABA and glutamate transporters in brain. *Front. Endocrinol.* **4**, 165 (2013).
47. Vaccarino, F. M. et al. Changes in cerebral cortex size are governed by fibroblast growth factor during embryogenesis. *Nat. Neurosci.* **2**, 246–253 (1999).
48. Pringle, N. P. et al. Fgfr3 expression by astrocytes and their precursors: evidence that astrocytes and oligodendrocytes originate in distinct neuroepithelial domains. *Development* **130**, 93–102 (2003).

Methods

Zebrafish husbandry and maintenance. Wild-type zebrafish (AB strain), *Tg[slc1a3b:myrGFP-P2A-H2AmCherry]* and *Tg[slc1a3b:myrGCaMP6s]* transgenic lines were used in this study. All zebrafish experiments and procedures were performed in compliance with institutional ethical regulations for animal testing and research at Oregon Health & Science University (OHSU). Experiments were approved by the Institutional Animal Care and Use Committee of OHSU. Zebrafish larvae and young fish were nurtured using rotifer suspension and dry food (Gemma 150). Adult fish were maintained and fed with a combination of brine shrimp, rotifer suspension and dry food (Gemma 300).

Plasmids and injections. To generate the *slc1a3b:myrGFP-P2A-H2AmCherry* reporter construct, the ~9.5-kb DNA sequence upstream of zebrafish *slc1a3b* translational start site was amplified from genomic DNA and subcloned into Tol2 vector pT2A_mini. The sequence encoding *myrGFP-P2A-H2AmCherry* was PCR amplified in two separate fragments and subsequently inserted in the 3′ end of the *slc1a3b* promoter. For the *slc1a3b:mCD8mCherry* construct, *slc1a3b* promoter and *mCD8mCherry* sequences were subcloned into Gateway vectors to generate *p5E-slc1a3b* and *pME-mCD8mCherry*, and Gateway LR reactions were performed to produce *slc1a3b:mCD8mCherry* in the *pDestTol2CG2* backbone. The *slc1a3b:myrGCaMP6s* construct was generated by replacing the *myrGFP* sequence in the *slc1a3b:myrGFP-P2A-H2AmCherry* construct with *myrGCaMP6s* using PCR. Tissue-specific CRISPR–Cas9 backbone vector *pDestTol2CG2-U6:gRNA* and *pME-Cas9* were purchased from Addgene. The *sgRNA*s targeting individual *fgfr* genes were designed using the online CRISPR toolbox CHOPCHOP[49]. Validated sgRNAs were then cloned into the *pDestTol2CG2-U6:gRNA* vector, and Gateway LR reactions were performed to recombine *slc1a3b* promoter and *Cas9* sequences. All constructs generated in this study were confirmed by Sanger sequencing (GENEWIZ) and are available upon request.

For mosaic analyses of individual cells, DNA constructs were injected into one-celled zygotes as follows: 20–30 pg of *slc1a3b:myrGFP-P2A-H2AmCherry*, 20–30 pg of *slc1a3b:mCD8mCherry* or 10–20 pg of *slc1a3b:nlsCas9nls;U6:sgRNA-fgfr1-4*. Injected embryos were kept at 28.5 °C until desired developmental stages for analysis.

In situ hybridization. For in situ hybridization probes, all gene-specific templates were PCR amplified with a T7 promoter sequence from 6-dpf wild-type complementary DNA. RNA probes were synthesized using Digoxigenin/Fluorescein RNA Labeling Kit (Sigma-Aldrich), except for the *kcnj10a* RNAscope probe, which was acquired from ACDBio. Whole-mount in situ hybridization was carried out as previously described[50]. Staged zebrafish embryos and larvae were fixed in 4% paraformaldehyde (PFA)/1× phosphate-buffered saline (PBS) at 4 °C overnight and dehydrated with 100% methanol at −20 °C overnight or longer. Samples were then rehydrated and treated with proteinase K (Bioline) to increase permeabilization. Pre-hybridization was subsequently performed at 65 °C in hybridization buffer (50% formamide, 5× SSC, 50 µg ml^{-1} heparin, 500 µg ml^{-1} transfer RNA, 100 mM citric acid and 0.1% Tween 20 in water) for at least 4 h and then incubated in digoxigenin/fluorescein probe containing hybridization buffer at 65 °C overnight. Anti-digoxigenin/fluorescein-AP antibody was used at 1:2,000–5,000 and followed by alkaline phosphatase staining protocol or Vector Red staining protocol (Vector Laboratories). RNAScope fluorescent in situ hybridization experiments for *kcnj10a* were performed using RNAScope Fluorescent Multiplex Assay Kit (ACDBio).

Generation of transgenic lines in zebrafish. To generate stable transgenic lines in zebrafish, we used the Tol2 transposon method, as described previously[51]. Then, 25 pg of synthetic RNA encoding *Tol2* transposase was co-injected with 10–20 pg of either *slc1a3b:myrGFP-P2A-H2AmCherry* or *slc1a3b:myrGCaMP6s* DNA into one-celled zygotes, and injected embryos were raised up to adulthood as the F_0 generation. To screen for transgenic-positive lines, F_0 fish were then out-crossed with wild-type AB fish and examined for F_1 progenies that were *slc1a3b:myrGFP-P2A-H2AmCherry*$^+$ or *slc1a3b:myrGCaMP6s*$^+$ during larval stages. Transgenic-positive F_1 carriers were further analyzed at adult stages to establish lines with a single-copy insertion and referred to as *Tg[slc1a3b:myrGFP-P2A-H2AmCherry]* or *Tg[slc1a3b:myrGCaMP6s]* in this study.

Confocal microscopy and live-imaging. Confocal imaging of live or stained zebrafish larvae was performed using an Innovative Imaging Innovations (3i) spinning-disk confocal microscope equipped with a Yokogawa CSX-X1 scan head. Super-resolution confocal analyses were performed using a Zeiss LSM 980 with Airyscan 2 confocal microscope.

For live-imaging, zebrafish larvae were anesthetized with 0.16 mg ml^{-1} of tricaine in embryo medium and mounted in 1.2% low-melting agarose on a cover slip with extra embryo medium sealed inside vacuum grease to prevent evaporation. Time-lapse Ca^{2+} imaging was performed on 6-dpf *Tg[slc1a3b:myrGCaMP6s]* larval spinal cord or hindbrain on a single *z* plane at 0.5-s intervals for 5–10 min. For drug treatment experiments, DMSO (0.1%) or NE (100 µM, Sigma-Aldrich) in embryo medium was used. For TTX injection experiments, 6-dpf *Tg[slc1a3b:myrGCaMP6s]* larvae were injected with 1 nl of 0.5 mM TTX into the yolk, and 10 min were allowed to elapse to confirm that the larvae were paralyzed. After 10 min and confirmation of paralysis, DMSO or NE was applied to the embryo medium, and larvae were incubated for 20–30 min before Ca^{2+} imaging, as described above.

Immunofluorescence staining. Zebrafish embryos and larvae were fixed in 4% PFA/1× PBS at 4 °C overnight and then incubated with 150 mM Tris-HCl, pH 9.0, at 70 °C for 15 min for antigen retrieval[52]. Samples were then permeabilized with 100% acetone at −20 °C for 20 min, and antibody staining was performed via standard procedures[50]. The following primary antibodies used: chicken α-GFP (Abcam, 1:1,000), rabbit α-RFP (Rockland, 1:1,000), mouse α-SV2 (DSHB, 1:200) and mouse α-GS (Sigma-Aldrich, 1:1 prediluted). The following secondary antibodies were used: Alexa 488 α-chicken (Jackson ImmunoResearch, 1:250), Rhodamine Red-X α-rabbit (Jackson ImmunoResearch, 1:250) and Dylight 649 α-mouse (Vector Laboratories, 1:250). Stained samples were mounted in Vectashield antifade mounting medium (Vector Laboratories) for confocal analysis.

Quantification and statistical analysis. Astrocyte cell territories or volumes were analyzed using Slidebook 6.0 or Imaris 8 (Bitplane) software. Ca^{2+} imaging data were analyzed with ImageJ 1.52p and AQuA 1.0 software, as described previously[34]. All statistical analyses were performed with GraphPad Prism 8 software. When comparing two groups, unpaired two-tailed Student's *t*-tests were used. One-way ANOVA was performed for multiple groups followed by Tukey's multiple comparisons test. See figure legends and text for specific statistical analyses used. No statistical methods were used to predetermine sample sizes, but our sample sizes are similar to those reported in previous publications[53–55]. Data distribution was assumed to be normal, and zebrafish embryos and larvae were randomly allocated to groups. Experiments were not performed blinded to the conditions of the experiments; data analyses were performed blinded to the scorer or did not require manual scoring.

Reporting Summary. Further information on research design is available in the Life Sciences Reporting Summary linked to this article.

Data availability

The data that support the findings of this study are available in the manuscript or the Supplementary Information. All reagents and additional data from this study are available upon reasonable request. Source data are provided with this paper.

References

49. Labun, K. et al. CHOPCHOP v3: expanding the CRISPR web toolbox beyond genome editing. *Nucleic Acids Res.* **47**, W171–W174 (2019).
50. Cunningham, R. L. & Monk, K. R. Whole mount in situ hybridization and immunohistochemistry for zebrafish larvae. *Methods Mol. Biol.* **1739**, 371–384 (2018).
51. Kawakami, K., Shima, A. & Kawakami, N. Identification of a functional transposase of the Tol2 element, an Ac-like element from the Japanese medaka fish, and its transposition in the zebrafish germ lineage. *Proc. Natl Acad. Sci. USA* **97**, 11403–11408 (2000).
52. Inoue, D. & Wittbrodt, J. One for all–a highly efficient and versatile method for fluorescent immunostaining in fish embryos. *PLoS ONE* **6**, e19713 (2011).
53. Ackerman, S. D., Garcia, C., Piao, X., Gutmann, D. H. & Monk, K. R. The adhesion GPCR Gpr56 regulates oligodendrocyte development via interactions with Galpha12/13 and RhoA. *Nat. Commun.* **6**, 6122 (2015).
54. Herbert, A. L. et al. Dynein/dynactin is necessary for anterograde transport of Mbp mRNA in oligodendrocytes and for myelination in vivo. *Proc. Natl Acad. Sci. USA* **114**, E9153–E9162 (2017).
55. Baraban, M., Koudelka, S. & Lyons, D. A. Ca^{2+} activity signatures of myelin sheath formation and growth in vivo. *Nat. Neurosci.* **21**, 19–23 (2018).

Acknowledgements

We thank S. Ackerman, D. Lyons and members of the Freeman and Monk labs for helpful discussions and comments on the manuscript. We are indebted to M. Cahill, S. Pittolo and M. Reitman of the Poskanzer lab for assistance with the AQuA software platform and to K. Cole of the Lyons lab for TTX experiment advice. We thank A. Forbes and G. Halsell-Vore for excellent zebrafish care and L. Vaskalis for graphics. This work was supported by R01NS099254 to K.E.P., R37NS053538 to M.R.F. and R21NS115437 to K.R.M.

Author contributions

J.C., M.R.F. and K.R.M. conceived the project. J.C. carried out experiments and data analyses. K.E.P. provided support for the AQuA software analyses. All authors contributed to the final version of the manuscript.

Competing interests
The authors declare no competing interests.

Additional information
Extended data is available for this paper at https://doi.org/10.1038/s41593-020-0703-x.

Supplementary information is available for this paper at https://doi.org/10.1038/s41593-020-0703-x.

Correspondence and requests for materials should be addressed to J.C. or K.R.M.

Reprints and permissions information is available at www.nature.com/reprints.

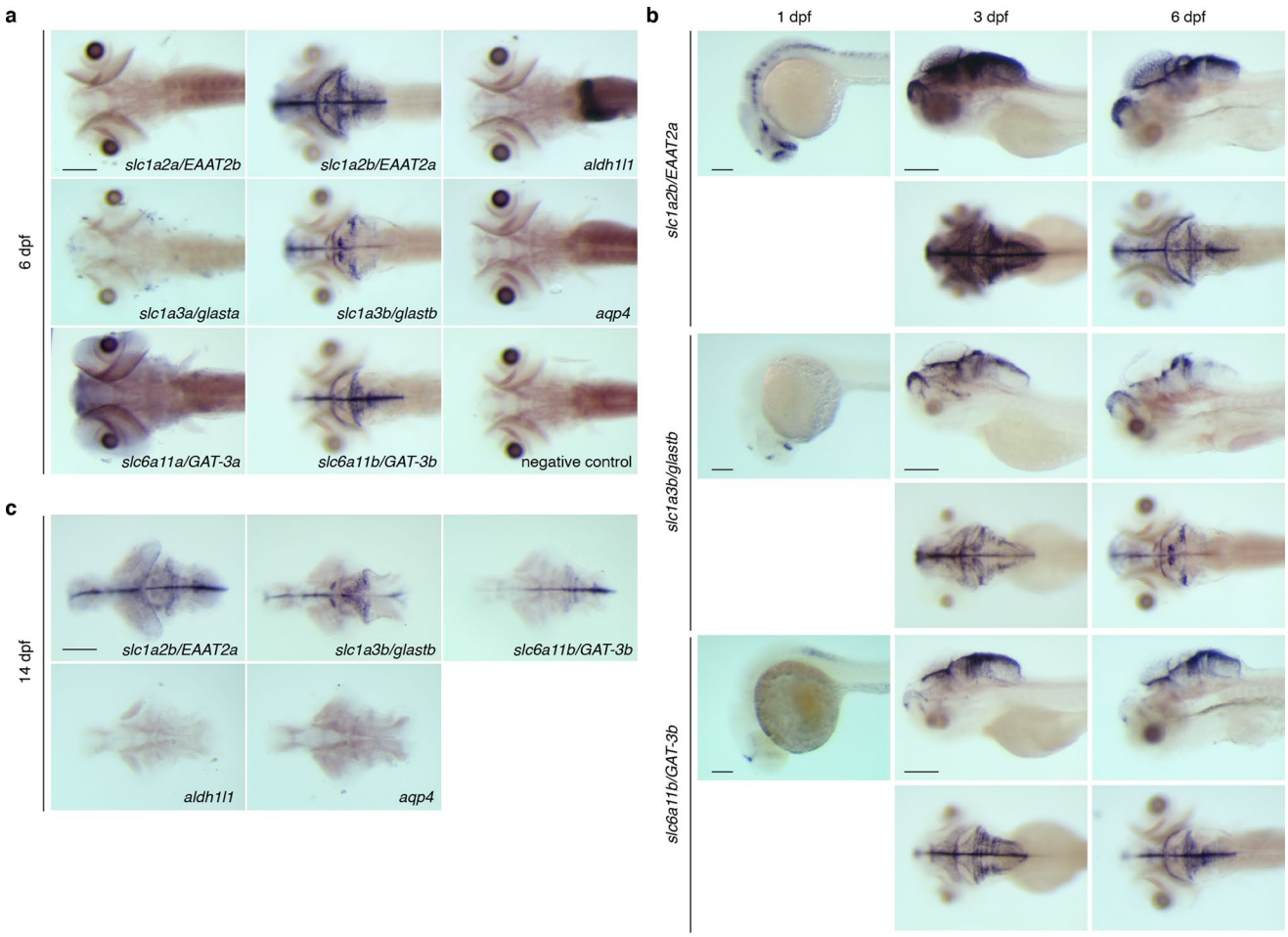

Extended Data Fig. 1 | Whole mount *in situ* hybridization of mammalian astrocyte markers in different stage zebrafish larvae. a, 6 dpf expression patterns of *slc1a2a/EAAT2b*, *slc1a2b/EAAT2a*, *slc1a3a/Glasta*, *slc1a3b/Glastb*, *slc6a11a/GAT-3a*, *slc6a11b/GAT-3b*, *aldh1l1*, and *aqp4*. **b**, Expression patterns of *slc1a2b/EAAT2a*, *slc1a3b/Glastb*, and *slc6a11b/GAT-3b* at 1 dpf, 3 dpf, and 6 dpf in lateral and dorsal view. **c**, Expression patterns of *slc1a2b/EAAT2a*, *slc1a3b/Glastb*, *slc6a11b/GAT-3b*, *aldh1l1*, and *aqp4* in 14 dpf dissected brains. Scale bar, 200 μm. All images are representative of three or four independent repeats.

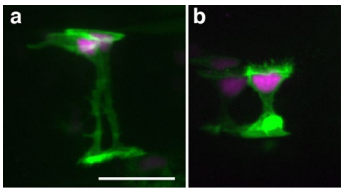

Extended Data Fig. 2 | slc1a3b:myrGFP-P2A-H2AmCherry-labeled RGCs and ependymal cells in 6 dpf zebrafish larvae. a, **b**, Representative images show RGCs (**a**) and ependymal cells (**b**) in zebrafish spinal cord labeled by the *slc1a3b:myrGFP-P2A-H2AmCherry* DNA construct. Scale bar, 20 μm. Representative images from three independent repeats.

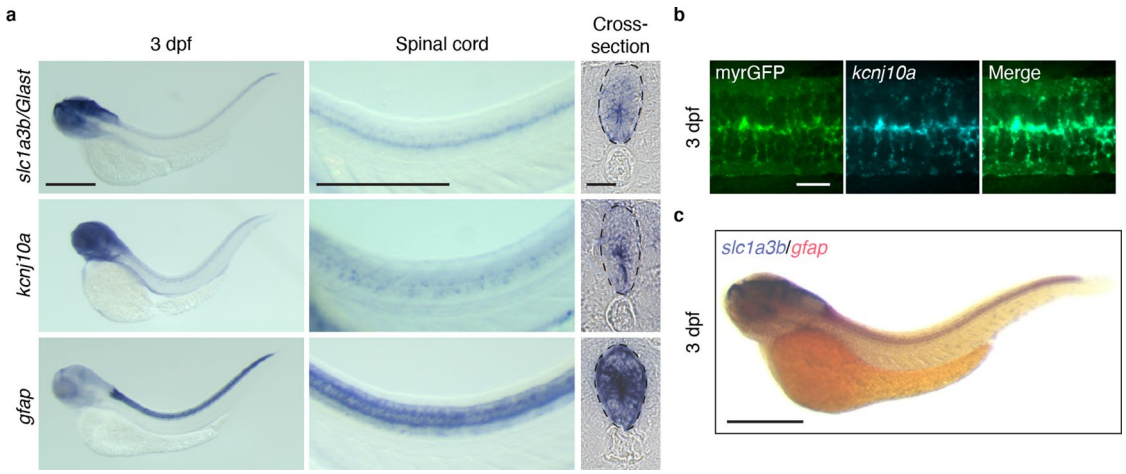

Extended Data Fig. 3 | *In situ* hybridization of *slc1a3b*, *kcnj10a/Kir4.1*, and *gfap* in 3 dpf larvae. a, Representative images show the comparison of *slc1a3b*, *kcnj10a/Kir4.1*, and *gfap* in the spinal cord. Dash lines mark the outline of spinal cord. Images are representative of N=3-4 fish larvae. Scale bars represent 500 μm for left panel, 200 μm for middle panel, and 20 μm for right panel, respectively. **b**, RNAScope *in situ* hybridization of *kcnj10a* in *Tg[slc1a3b:myrGFP-P2A-H2AmCherry]* fish spinal cord at 3 dpf. Single z-plane, dorsal view. Scale bar, 20 μm. Representative images from N=3 fish larvae. **c**, Double staining *in situ* hybridization of *slc1a3b* (purple) and *gfap* (red) at 3 dpf. Scale bar, 500 μm. Representative images from N=6 fish larvae.

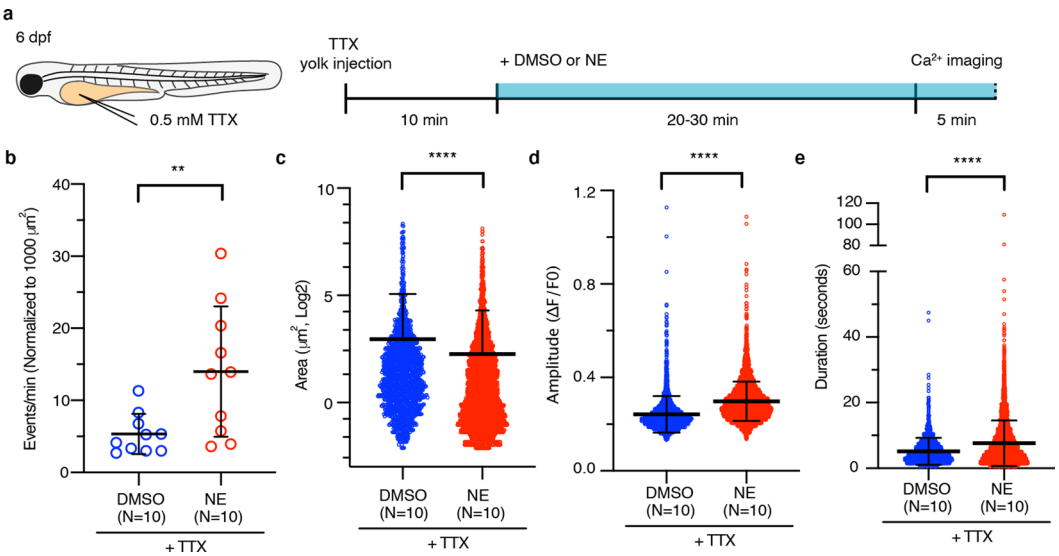

Extended Data Fig. 4 | NE-induced Microdomain Ca^{2+} transients in spinal cord astrocytes are not driven by neuronal activity. a, Schematic overview of the TTX injection experiments. **b-e**, Comparisons of average microdomain Ca^{2+} events frequencies (**b**), area sizes (**c**), amplitudes (**d**), and durations (**e**) in DMSO control and NE-treated fish following TTX injections. Error bars represent Mean values +/- SD. **, p<0.01; ****, p<0.0001. p=0.0094 (**b**), p=1.07×10^{-7} (**c**), p<1.0×10^{-15} (**d** and **e**). Two-tailed unpaired *t* test. N, number of fish analyzed.

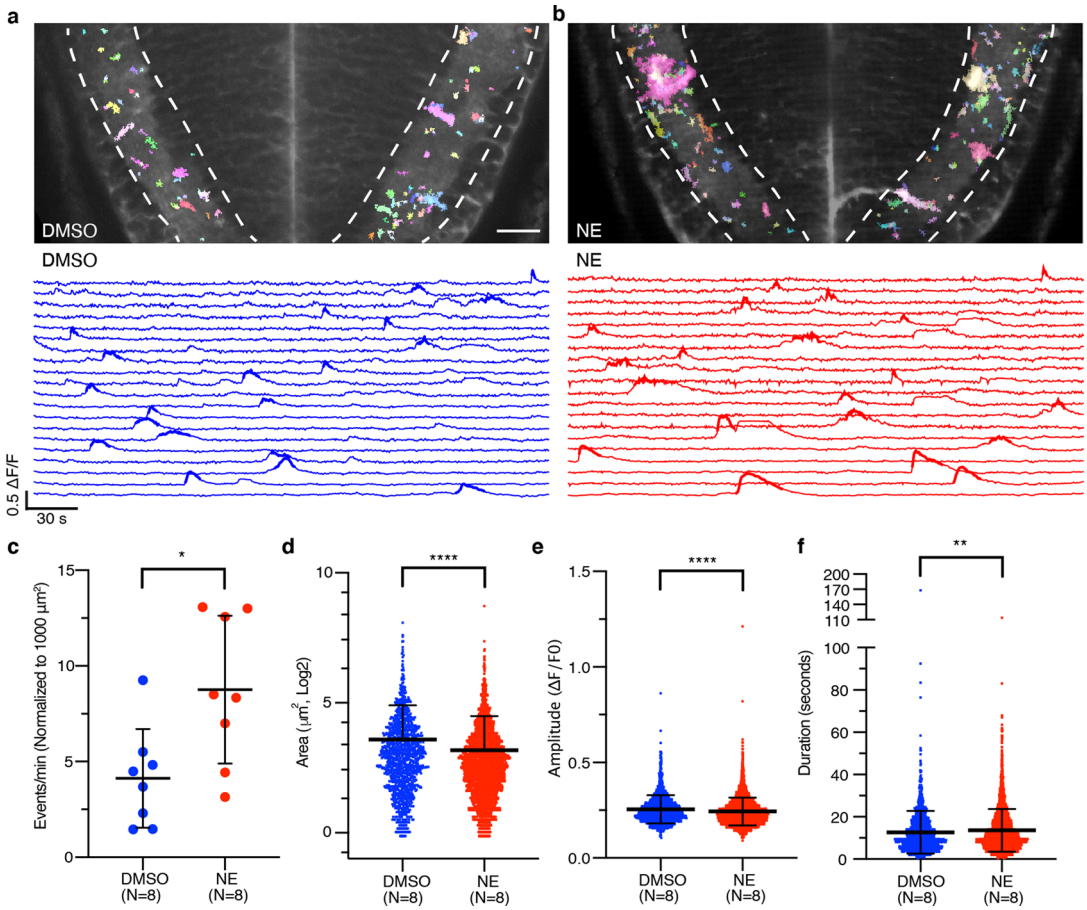

Extended Data Fig. 5 | Microdomain Ca^{2+} transients in the hindbrain radial astrocytes are sensitive to NE treatment. a, **b**, AQuA-detected Ca^{2+} events in DMSO control versus NE-treated *Tg[slc1a3b:myrGCaMP6s]* fish hindbrain radial astrocytes, and corresponding 20 individual ΔF/F traces. Scale bar, 20 μm. Dashed lines mark the regions representing the fine cellular processes of radial astrocytes that were analyzed. See also Supplementary Videos 6 and 7. **c-f**, Quantifications of average microdomain Ca^{2+} events frequency, area size, amplitude, and duration in DMSO control and NE-treated fish hindbrain regions. Error bars represent mean values +/- SD. *, p<0.05; **, p<0.01; ****, p<0.0001. p=0.0136 (**c**), p=4.43×10^{-9} (**d**), p=6.55×10^{-6} (**e**), p=0.0058 (**f**). Two-tailed unpaired *t* test. N, number of fish analyzed.

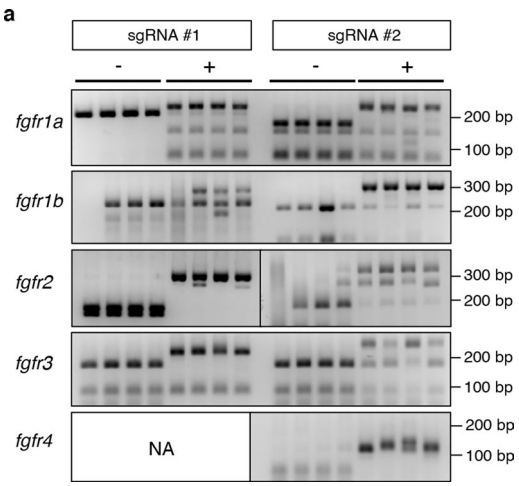

Extended Data Fig. 6 | Designed sgRNAs targeting *fgfr1-4* are effective in disrupting corresponding genes. a, Genotyping PCR results show that the co-injections of individual *sgRNAs* together with Cas9 protein led to the disruptions of endogenous restriction enzyme sites in contrast to uninjected controls. Two independent sgRNAs were tested except for *fgfr4*. NA, not available due to high toxicity.

nature research

Corresponding author(s): Jiakun Chen, Kelly Monk

Last updated by author(s): Jul 17, 2020

Reporting Summary

Nature Research wishes to improve the reproducibility of the work that we publish. This form provides structure for consistency and transparency in reporting. For further information on Nature Research policies, see our Editorial Policies and the Editorial Policy Checklist.

Statistics

For all statistical analyses, confirm that the following items are present in the figure legend, table legend, main text, or Methods section.

n/a	Confirmed	
☐	☒	The exact sample size (*n*) for each experimental group/condition, given as a discrete number and unit of measurement
☒	☐	A statement on whether measurements were taken from distinct samples or whether the same sample was measured repeatedly
☐	☒	The statistical test(s) used AND whether they are one- or two-sided *Only common tests should be described solely by name; describe more complex techniques in the Methods section.*
☒	☐	A description of all covariates tested
☒	☐	A description of any assumptions or corrections, such as tests of normality and adjustment for multiple comparisons
☐	☒	A full description of the statistical parameters including central tendency (e.g. means) or other basic estimates (e.g. regression coefficient) AND variation (e.g. standard deviation) or associated estimates of uncertainty (e.g. confidence intervals)
☐	☒	For null hypothesis testing, the test statistic (e.g. *F*, *t*, *r*) with confidence intervals, effect sizes, degrees of freedom and *P* value noted *Give P values as exact values whenever suitable.*
☒	☐	For Bayesian analysis, information on the choice of priors and Markov chain Monte Carlo settings
☒	☐	For hierarchical and complex designs, identification of the appropriate level for tests and full reporting of outcomes
☒	☐	Estimates of effect sizes (e.g. Cohen's *d*, Pearson's *r*), indicating how they were calculated

Our web collection on statistics for biologists contains articles on many of the points above.

Software and code

Policy information about availability of computer code

Data collection	slidebook 6.0, Zeiss 3.0
Data analysis	CHOPCHOP (https://chopchop.cbu.uib.no), ImageJ 1.52p, slidebook 6.0, Imaris 8, AQuA 1.0, Prism 8

For manuscripts utilizing custom algorithms or software that are central to the research but not yet described in published literature, software must be made available to editors and reviewers. We strongly encourage code deposition in a community repository (e.g. GitHub). See the Nature Research guidelines for submitting code & software for further information.

Data

Policy information about availability of data

All manuscripts must include a data availability statement. This statement should provide the following information, where applicable:

- Accession codes, unique identifiers, or web links for publicly available datasets
- A list of figures that have associated raw data
- A description of any restrictions on data availability

The data that support the findings of this study are available from the corresponding author upon reasonable request.

Field-specific reporting

Please select the one below that is the best fit for your research. If you are not sure, read the appropriate sections before making your selection.

☒ Life sciences ☐ Behavioural & social sciences ☐ Ecological, evolutionary & environmental sciences

For a reference copy of the document with all sections, see nature.com/documents/nr-reporting-summary-flat.pdf

Life sciences study design

All studies must disclose on these points even when the disclosure is negative.

Sample size	No statistical methods were used to predetermine sample sizes, but our sample sizes were similar to those reported in previous studies (Ackerman et al., 2015; Herbert et al., 2017; Baraban et al., 2018).
Data exclusions	No data was excluded from the analysis.
Replication	All data were confirmed with at least 2 experimental repeats, and similar results were concluded.
Randomization	Fish embryos and larvae were randomly allocated into groups for all experiments.
Blinding	Experiments were not performed blind to the conditions of the experiments, data analyses were performed blinded to the scorer or did not require manual scoring.

Reporting for specific materials, systems and methods

We require information from authors about some types of materials, experimental systems and methods used in many studies. Here, indicate whether each material, system or method listed is relevant to your study. If you are not sure if a list item applies to your research, read the appropriate section before selecting a response.

Materials & experimental systems

n/a	Involved in the study
☐	☒ Antibodies
☒	☐ Eukaryotic cell lines
☒	☐ Palaeontology and archaeology
☐	☒ Animals and other organisms
☒	☐ Human research participants
☒	☐ Clinical data
☒	☐ Dual use research of concern

Methods

n/a	Involved in the study
☒	☐ ChIP-seq
☒	☐ Flow cytometry
☒	☐ MRI-based neuroimaging

Antibodies

Antibodies used	Chicken anti-GFP (Abcam, ab13970), rabbit anti-RFP (Rockland, 600-401-379), mouse anti-SV2 (DSHB, AB 2315387), mouse anti-GS (Sigma, 389M), Alexa 488 anti-chicken(Jackson ImmunoResearch, 703-545-155), Rhodamine Red-X -rabbit (Jackson ImmunoResearch, 111-295-003), and Dylight 649 anti-mouse (Vector Laboratories, DI-2649), anti-Digoxigenin-AP (Sigma, 11093274910), anti-Fluorescein-AP (Sigma, 11426338910)
Validation	Chicken anti-GFP and rabbit anti-RFP antibodies has been used in zebrafish for immunostaining (Lessen et al., 2017); mouse anti-SV2 antibody has been used in zebrafish for immunostaining (Turner et al., 2014); For mouse anti-GS antibody, same clone antibody (GS-6)from Chemicon (MAB302) has been used in zebrafish for immunostaining (Grupp et al., 2010).

Animals and other organisms

Policy information about studies involving animals; ARRIVE guidelines recommended for reporting animal research

Laboratory animals	Zebrafish at 1-14 days post-fertilization were used for all experiments in this study. Sex could not be determined at this stage of zebrafish.
Wild animals	No wild animals were used in this study.
Field-collected samples	No field-collected samples were used in this study.
Ethics oversight	Institutional Animal Care and Use Committee of OHSU

Note that full information on the approval of the study protocol must also be provided in the manuscript.